

# *NUSTAR* UNVEILS A HEAVILY OBSCURED LOW-LUMINOSITY ACTIVE GALACTIC NUCLEUS IN THE LUMINOUS INFRARED GALAXY NGC 6286

C. RICCI<sup>1,2,\*</sup>, F. E. BAUER<sup>1,2,3,4</sup>, E. TREISTER<sup>5,2</sup>, C. ROMERO-CANIZALES<sup>1,3</sup>, P. AREVALO<sup>6</sup>, K. IWASAWA<sup>7</sup>, G. C. PRIVON<sup>5</sup>,  
D. B. SANDERS<sup>8</sup>, K. SCHAWINSKI<sup>9</sup>, D. STERN<sup>10</sup>, M. IMANISHI<sup>11,12,13</sup>

*Draft version January 25, 2016*

## ABSTRACT

We report the detection of a heavily obscured Active Galactic Nucleus (AGN) in the luminous infrared galaxy (LIRG) NGC 6286, identified in a 17.5 ks *NuSTAR* observation. The source is in an early merging stage, and was targeted as part of our ongoing *NuSTAR* campaign observing local luminous and ultra-luminous infrared galaxies in different merger stages. NGC 6286 is clearly detected above 10 keV and, by including the quasi-simultaneous *Swift*/XRT and archival *XMM-Newton* and *Chandra* data, we find that the source is heavily obscured [ $N_{\text{H}} \simeq (0.95 - 1.32) \times 10^{24} \text{ cm}^{-2}$ ], with a column density consistent with being Compton-thick [CT,  $\log(N_{\text{H}}/\text{cm}^{-2}) \geq 24$ ]. The AGN in NGC 6286 has a low absorption-corrected luminosity ( $L_{2-10 \text{ keV}} \sim 3 - 20 \times 10^{41} \text{ erg s}^{-1}$ ) and contributes  $\lesssim 1\%$  to the energetics of the system. Because of its low-luminosity, previous observations carried out in the soft X-ray band ( $< 10 \text{ keV}$ ) and in the infrared did not notice the presence of a buried AGN. NGC 6286 has multi-wavelength characteristics typical of objects with the same infrared luminosity and in the same merger stage, which might imply that there is a significant population of obscured low-luminosity AGN in LIRGs that can only be detected by sensitive hard X-ray observations.

**Keywords:** galaxies: active — X-rays: general — galaxies: interactions — X-rays: galaxies — infrared: galaxies

## 1. INTRODUCTION

Luminous [ $L_{\text{IR}}(8 - 1000 \mu\text{m}) = 10^{11} - 10^{12} L_{\odot}$ ] and ultra-luminous ( $L_{\text{IR}} \geq 10^{12} L_{\odot}$ ) infrared galaxies (LIRGs and ULIRGs, respectively) were first discovered in the late sixties (Low & Kleinmann 1968; Kleinmann & Low 1970). With the advent of the *Infrared Astronomical Satellite* (*IRAS*, see Sanders & Mirabel 1996 for a review), which discovered a large number of U/LIRGs, the cosmological importance of these objects became evident. Although they are relatively rare at low redshift, their luminosity function is very steep (Le Floc'h et al. 2005),

and they are the major contributor to the IR energy density at  $z \simeq 1 - 2$  (e.g., Caputi et al. 2007, Goto et al. 2010).

The discovery that most, if not all, U/LIRGs are triggered by galaxy mergers led to the development of an evolutionary scenario (Sanders et al. 1988) in which two gas rich disk galaxies collide, triggering an intense phase of star formation in which they are observed as U/LIRGs. This is then followed by a blowout phase, during which most of the material enshrouding the supermassive black hole (SMBH) is blown away and the system is observed as a luminous red quasar (e.g., Glikman et al. 2015 and references therein). When most of the dust is removed, the system is eventually observed as a blue quasar. This model is consistent with the observed increase of the fraction of obscured sources with redshift up to  $z \simeq 3$  (Treister et al. 2010a; Ueda et al. 2014). The *Wide-field Infrared Survey Explorer* satellite (*WISE*) has recently found evidence of a new population of very luminous IR sources ( $L_{\text{IR}} > 10^{13} L_{\odot}$ ), dubbed Hot Dust Obscured Galaxies (Hot DOGs, Wu et al. 2012), which might represent a short evolutionary phase in the evolution of galaxies, and be related to mergers (e.g., Eisenhardt et al. 2012; Stern et al. 2014; Assef et al. 2015). Numerical simulations (e.g., Springel et al. 2005) have also shown that tidal interactions can drive an inflow of material that triggers and feeds both accretion onto the SMBH and star formation. Therefore, mergers might play an important role in fuelling the SMBH, as it has been suggested by the discovery that the fraction of active galactic nuclei (AGN) in mergers increases with the AGN luminosity (Treister et al. 2012; Schawinski et al. 2012), spanning from  $< 1\%$  at a 2–10 keV luminosity of  $L_{2-10} \sim 10^{41} \text{ erg s}^{-1}$  to 70–80% in the most luminous quasars with

<sup>1</sup> Instituto de Astrofísica, Facultad de Física, Pontificia Universidad Católica de Chile, Casilla 306, Santiago 22, Chile

<sup>2</sup> EMBIGGEN Anillo

<sup>3</sup> Millennium Institute of Astrophysics, Chile

<sup>4</sup> Space Science Institute, 4750 Walnut Street, Suite 205, Boulder, Colorado 80301, USA

<sup>5</sup> Universidad de Concepción, Departamento de Astronomía, Casilla 160-C, Concepción, Chile

<sup>6</sup> Instituto de Física y Astronomía, Facultad de Ciencias, Universidad de Valparaíso, Gran Bretaña N 1111, Playa Ancha, Valparaíso, Chile.

<sup>7</sup> ICREA and Institut de Ciències del Cosmos, Universitat de Barcelona, IEEC-UB, Martí i Franquès, 1, 08028 Barcelona, Spain

<sup>8</sup> Institute for Astronomy, 2680 Woodlawn Drive, University of Hawaii, Honolulu, HI 96822

<sup>9</sup> Institute for Astronomy, Department of Physics, ETH Zurich, Wolfgang-Pauli-Strasse 27, CH-8093 Zurich, Switzerland

<sup>10</sup> Jet Propulsion Laboratory, California Institute of Technology, Pasadena, CA 91109, USA

<sup>11</sup> Subaru Telescope, 650 North A'ohoku Place, Hilo, Hawaii, 96720, U.S.A.

<sup>12</sup> National Astronomical Observatory of Japan, 2-21-1 Osawa, Mitaka, Tokyo 181-8588, Japan

<sup>13</sup> Department of Astronomical Science, The Graduate University for Advanced Studies (SOKENDAI), Mitaka, Tokyo 181-8588, Japan

\* cricci@astro.puc.cl



**Figure 1.** Optical image of the interacting pair NGC 6286 (bottom)/NGC 6285 (top) obtained with the Schulman 32-inch Telescope of the Mount Lemmon SkyCenter. Image courtesy of Adam Block (Mount Lemmon SkyCenter/University of Arizona).

$$L_{2-10} \sim 10^{46} \text{ erg s}^{-1}.$$

The contribution of AGN to the overall luminosity of U/LIRGs has been shown to increase with the IR luminosity of the system (e.g., Veilleux et al. 1995, 1999; Imanishi 2009; Imanishi et al. 2010a,b; Nardini et al. 2010; Alonso-Herrero et al. 2012; Ichikawa et al. 2014). Due to the great opacity of the nuclear region, a clear identification of AGN in U/LIRGs is often complicated. Mid-IR (MIR) properties have been used to estimate the relative contribution of accretion onto the SMBH and star formation to the bolometric luminosity. This has been done by exploiting  $5\text{--}8\mu\text{m}$  spectroscopy (e.g., Nardini et al. 2010), and the characteristics of several features in the  $L$  ( $3\text{--}4\mu\text{m}$ ) and  $M$  ( $4\text{--}5\mu\text{m}$ ) bands (Imanishi & Dudley 2000; Risaliti et al. 2006; Sani et al. 2008; Risaliti et al. 2010): the  $3.3\mu\text{m}$  polycyclic aromatic hydrocarbon (PAH) emission feature, the bare carbonaceous  $3.4\mu\text{m}$  absorption feature, and the slope of the continuum. The  $6.2\mu\text{m}$  (e.g., Stierwalt et al. 2013, 2014) and  $7.7\mu\text{m}$  PAH features (e.g., Veilleux et al. 2009), the presence of high-excitation MIR lines (e.g., [Ne V]  $14.32\mu\text{m}$ , Veilleux et al. 2009), or the radio properties (e.g., Parra et al. 2010, Romero-Cañizales et al. 2012a, Vardoulaki et al. 2015) have also been used to infer the presence of a buried AGN.

X-ray observations are a very powerful tool to detect accreting SMBHs and to disentangle the contributions of star formation and AGN emission to the total luminosity of U/LIRGs. Studies performed so far using *XMM-Newton* (e.g., Franceschini et al. 2003; Imanishi et al. 2003; Pereira-Santaella et al. 2011) and *Chandra* (e.g., Ptak et al. 2003; Teng et al. 2005; Iwasawa et al. 2011) have characterized the properties of a significant number of these systems. However, a significant fraction of U/LIRGs might be heavily obscured (e.g., Treister et al. 2010b; Bauer et al. 2010), and X-rays at energies  $\lesssim 10\text{ keV}$  are strongly attenuated in Compton-thick (CT,  $N_{\text{H}} \geq 10^{24} \text{ cm}^{-2}$ ) AGN. Observations carried out in the hard X-ray band ( $\geq 10\text{ keV}$ ) are less affected by absorption, and can be used to probe nuclear X-ray emission even in highly obscured systems (e.g., Baloković et al. 2014, Gandhi et al. 2014,

Arévalo et al. 2014, Bauer et al. 2015, Koss et al. 2015, Lansbury et al. 2015, Annular et al. 2015, Puccetti et al. 2015, Ricci et al. 2015). Previous hard X-ray observations of U/LIRGs have been carried out with *BeppoSAX* (e.g., Vignati et al. 1999), *Suzaku* (e.g., Teng et al. 2009) and *Swift*/BAT (Koss et al. 2013).

The recent launch of the *Nuclear Spectroscopic Telescope Array* (*NuSTAR*, Harrison et al. 2013), the first focussing telescope in orbit operating at  $E \geq 10\text{ keV}$ , has opened a new window in the study of U/LIRGs thanks to its unprecedented characteristics. The first studies of the hard X-ray emission of local ULIRGs carried out with *NuSTAR* have recently been reported by Teng et al. (2015) and Ptak et al. (2015), who show the importance of sensitive hard X-ray spectra to well constrain the line-of-sight column density.

We report here on the first results of a series of *NuSTAR* observations awarded to our group during AO-1 as a part of a campaign aimed at observing ten local LIRGs in different merger stages (PI: F. E. Bauer). The sources were selected from the Great Observatories All-sky LIRG Survey (GOALS<sup>15</sup>, Armus et al. 2009). GOALS is a local ( $z < 0.088$ ) sample which contains 181 LIRGs and 21 ULIRGs selected from the *IRAS* Revised Bright Galaxy Sample (Sanders et al. 2003).

This paper reports the detection of a heavily obscured AGN in NGC 6286 (also referred to as NGC 6286S), a LIRG ( $\log L_{\text{IR}}/L_{\odot} = 11.36$ , Howell et al. 2010) located at  $z = 0.018349$  (i.e., a luminosity distance of  $d_L = 76.1\text{ Mpc}$ ), which was not previously detected above  $10\text{ keV}$  (Koss et al. 2013). The source has a star-formation rate (SFR) of  $41.3 M_{\odot} \text{ yr}^{-1}$  (Howell et al. 2010), is in an early merging stage (i.e., stage *B* or 2, following the classification of Stierwalt et al. 2013), and is interacting with the galaxy NGC 6285 (NGC 6286N), located at a distance of  $\sim 1.5\text{ arcmin}$  ( $\sim 33\text{ kpc}$ , projected distance, see Fig. 1 and panel four of Fig. 2). The source is also known to host a OH megamaser (Baan et al. 1998). The only previous X-ray study of this source, carried out using *XMM-Newton* observations, did not find any evidence of an AGN (Brightman & Nandra 2011). The *XMM-Newton* can in fact be well represented by a model taking into account only a collisionally-ionized plasma and an unabsorbed power-law component, representing thermal emission from the starburst and X-ray radiation produced by X-ray binaries, respectively. Possible evidence of very faint AGN activity has been found studying the near-IR to radio spectral energy distribution (SED) (Vega et al. 2008), and could be inferred by the detection of [Ne V] lines, although the detection of these features has been questioned by Inami et al. (2013), and due to their weakness they might also be produced by a young starburst.

The paper is structured as follows. In § 2 and § 3 we present the X-ray and radio data used and describe the data reduction procedures, in § 4 we report on the X-ray spectral analysis of NGC 6286, in § 5 we discuss our results by taking into account the multi-wavelength properties of NGC 6286, and in § 6 we summarise the main results of our work. Throughout the paper we adopt standard cosmological parameters ( $H_0 = 70\text{ km s}^{-1} \text{ Mpc}^{-1}$ ,  $\Omega_{\text{m}} = 0.3$ ,  $\Omega_{\Lambda} = 0.7$ ).

<sup>15</sup> <http://goals.ipac.caltech.edu>

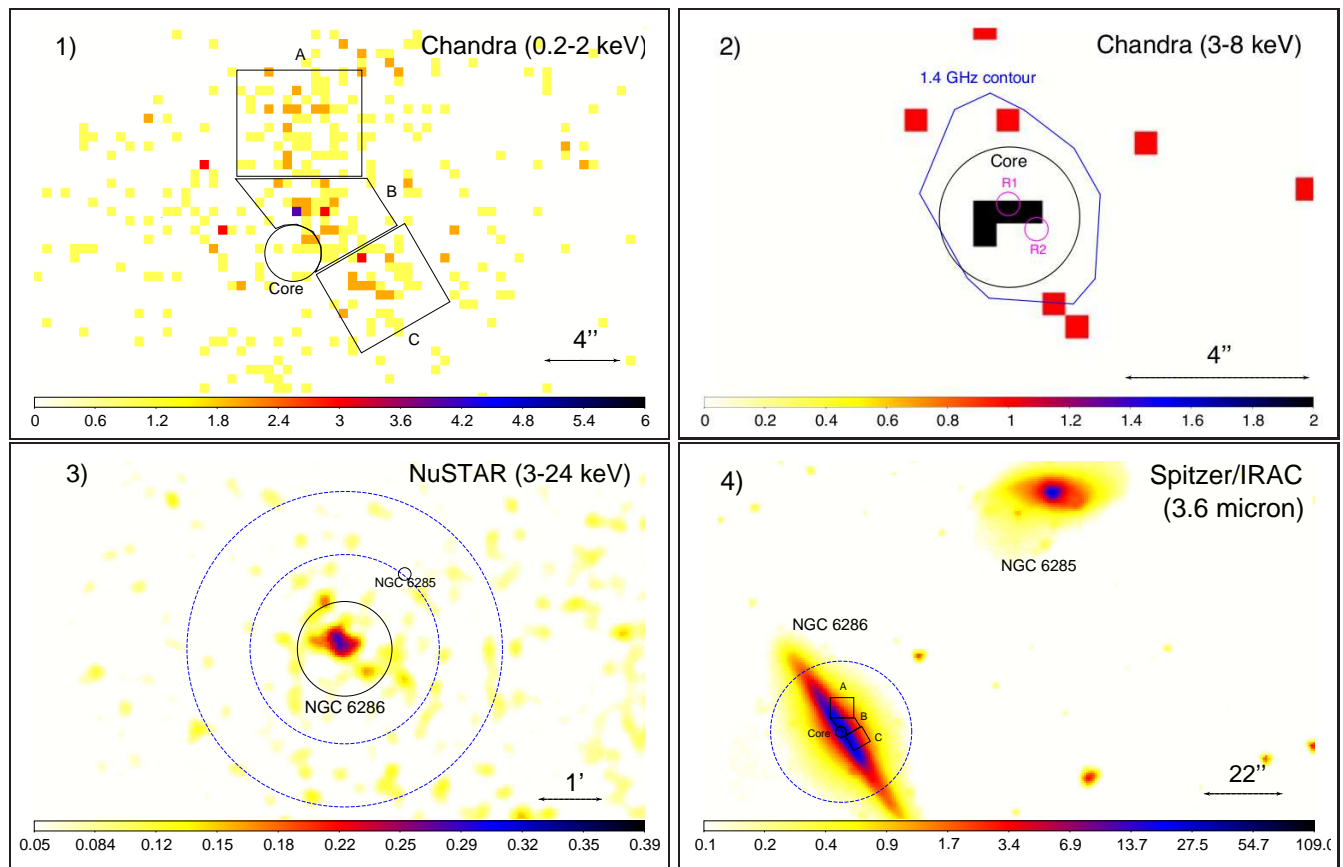


**Figure 2.** *Chandra* ACIS-S (panel one, 0.2–2 keV; panel two, 3–8 keV), *NuSTAR* FPMA (panel three, 3–24 keV) and *Spitzer* IRAC (panel four, 3.6  $\mu$ m) images of NGC 6286. The *Chandra* 0.2–2 keV image shows a clear extended structure of  $\sim 12$  arcsec size ( $\sim 4.4$  kpc). The four regions shown in panels one and four represent the 3–8 keV core, the north, central, and south regions discussed in § 4.1. The 1.4 GHz VLA FIRST radio contour is illustrated in panel two, together with the two radio sources (R1 and R2) detected by our analysis of EVN observations at 5 GHz (see § 3), which show that the radio emission coincides with the hard X-ray core, suggesting the presence of a buried AGN. The black circle and the blue dashed annulus in panel three correspond to the *NuSTAR* source and background extraction regions, respectively. The image in panel four was smoothed with a Gaussian kernel of radius 5 pixels. The blue dashed circle in panel four represents the source region used for *XMM-Newton* EPIC/PN.

## 2. X-RAY OBSERVATIONS AND DATA REDUCTION

### 2.1. *NuSTAR*

*NuSTAR* observed NGC 6286 on UT 2015 May 29 for 17.5 ks. We processed the data using the *NuSTAR* Data Analysis Software NUSTARDAS v1.4.1 within HEASOFT v6.16, adopting the latest calibration files (Madsen et al. 2015). The source is clearly detected in the 3–24 keV image (panel three of Fig. 2). For both focal plane modules (FPMA and FPMB) we extracted source and background spectra and light-curves with the NUPRODUCTS task. A circular region of 45 arcsec was used for the source<sup>16</sup>, while the background was extracted from an annulus centred on the X-ray source, with inner and outer radii of 90 and 150 arcsec, respectively. The 3–10 and 10–50 keV light-curves of the sources do not show any evidence of flux variability.

### 2.2. *XMM-Newton*

Two *XMM-Newton* (Jansen et al. 2001) observations of NGC 6286 (ID: 0203390701 and 0203391201; PI: Maiolino) were carried out on UT 2005 May 7, with

<sup>16</sup> In the 3–24 keV band for photon indices  $\Gamma = 0.6 - 1.8$  this aperture encloses  $\sim 65\%$  of the full PSF energy (Lansbury et al. 2015).

exposures of 20.8 and 8.9 ks. Both PN (Strüder et al. 2001) and MOS (Turner et al. 2001) data were analysed by reducing first the observation data files (ODFs) using the *XMM-Newton* Standard Analysis Software (SAS) version 12.0.1 (Gabriel et al. 2004), and then the raw PN and MOS data files using the EPCHAIN and EMCHAIN tasks, respectively. In order to filter the observations for periods of high background activity we analyzed the EPIC/PN and MOS background light curves in the 10–12 keV band and above 10 keV, respectively, and found that both observations show a significant background contamination. Observation 0203391201 was not used because the background flux dominates the whole observation (with an average count-rate of 6  $\text{cts s}^{-1}$  and a minimum of 2  $\text{cts s}^{-1}$ ). Observation 0203390701 showed less contamination, and we filtered the periods of high background activity using a threshold of 2  $\text{cts s}^{-1}$  for both PN and MOS, which resulted in net exposure times of 2.3 and 4.7 ks, respectively. For both cameras we extracted the spectrum of the source using a circular region of 20 arcsec radius, while the background was extracted from a circular region of 40 arcsec radius, located on the same CCD of the source and in a zone devoid of other sources. No significant flux variability is found in the 0.3–10 keV band during the *XMM-Newton* observation.



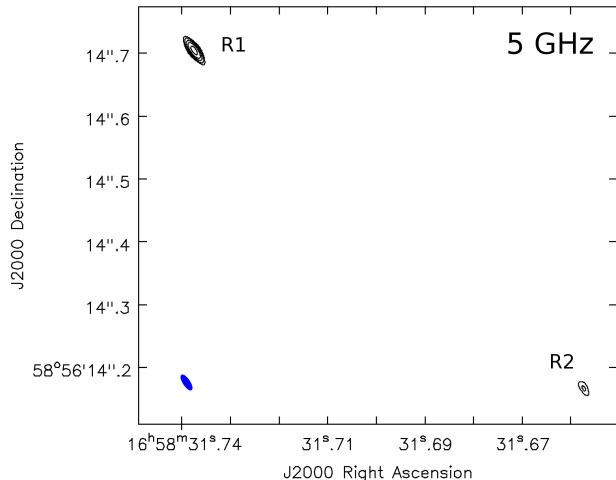


**Figure 3.** EVN (Effelsberg, Westerbork and Lovell antennas) contour map of NGC 6286 at 5 GHz from UT 2005 June 13, imaged with a convolving beam of  $8.39 \times 25.94$  arcsec at  $33.71^\circ$  (North through East) using natural weighting.

### 2.3. *Swift*/XRT

The X-ray Telescope (XRT, 0.2–10 keV; Burrows et al. 2005) on board *Swift* (Gehrels et al. 2004) observed NGC 6286 quasi-simultaneously with *NuSTAR* on UT 2015 May 29 for 2 ks. XRT data were reduced using the XRTPIPELINE v0.13.0 within HEASOFT v6.16.

### 2.4. *Chandra*

A *Chandra* (Weisskopf et al. 2000) ACIS-S (Garmire et al. 2003) observation of NGC 6286 was carried out on UT 2009 September 18 (PI: Swartz) with an exposure of 14.2 ks. The data reduction was performed following the standard procedure, using CIAO v4.6. The data were reprocessed using CHANDRA\_REPRO, and then the spectra were extracted using the SPEXTRACT tool.

The 0.2–2 keV *Chandra* image shows clear evidence of extended emission (panel one of Fig. 2). The 3–8 keV image (panel two) shows instead only a point-like source, which does not appear in the 0.2–2 keV image. This source is located at the center of the galaxy (see panel three) and could be associated with AGN emission. The spectra of these different regions are discussed in § 4.1.

In order to be consistent with the spectral extraction of *XMM-Newton* and *Swift*/XRT, which have a much lower spatial resolution than *Chandra*, the ACIS-S source spectrum used for the broad-band X-ray fitting was extracted from a circular region of 10.5 arcsec radius. The background spectrum was extracted from a circular region of the same size on the same CCD, where no other source was detected.

## 3. RADIO OBSERVATIONS AND DATA REDUCTION

Parra et al. (2010) reported VLA observations of NGC 6286 at 4.8 GHz, showing a compact morphology with a size of  $0.25 \times 0.21$  arcsec and a flux density of 15.24 mJy. They also observed this galaxy with three of the most sensitive antennas (Effelsberg, Westerbork and Lovell) of the European very long baseline interferometry (VLBI) Network (EVN) at 5 GHz, and detected fringes in each one of the baselines with amplitudes between 5.36–6.11 mJy. We have extracted these observations from the

archive and applied the pipelined calibration available. In Figure 3 we show the contour map obtained using the cleaning algorithm within the Caltech program DIFMAP (Shepherd et al. 1995). No proper flux density could be obtained with such a small array since the measurements are still subject of instrumental amplitude errors. We can however rely on the source structure, as there is enough information to determine phase closure. We find two milli-arcsec sources with  $S/N > 5$ , one (R1) at RA =  $16^h58^m31.7374^s$ , DEC =  $+58^\circ56'14.705''$ , and the other (R2) at RA =  $16^h58^m31.6572^s$ , DEC =  $+58^\circ56'14''.167$ . These two sources are consistent with the 3–8 keV core region (see panel two of Fig. 2 and § 4.1).

We have also extracted and analysed the very long baseline array (VLBA) experiment BC196 observed at 8 GHz on UT 2012 January 12. We used the NRAO Astronomical Image Processing System (AIPS) to reduce the data, following standard procedures. We note that the source chosen as phase reference (J1651+5805) is not detected in this experiment, and constraints for it are also not available in the VLBA Calibrator search engine at NRAO. We have resorted to the use of another nearby calibrator (J1656+6012, at  $2.22^\circ$ ) which was observed 2 min before the NGC 6286 scan. We found that there are no sources detected above  $\sim 0.8$  mJy/beam ( $3 \times \text{r.m.s.}$ ) in the VLBA observations convolved with a  $3.16 \times 0.94$  arcsec at  $29.31^\circ$  beam. If any of the sources detected with the EVN is the AGN core, we would expect a similar peak intensity measured in a baseline with comparable length as that from Ef-Jb or Ef-Wb baselines. The fact that we do not detect any source in the VLBA observations leaves two possible explanations: i) the sources are variable and the VLBA observations are not sensitive enough; ii) the sources are resolved at resolutions better than  $\sim 3$  arcsec. Although the VLBA array includes three times as much antennas as the EVN small array, it also observed the target for only 1/3 of the time with respect to the EVN, and using antennas  $\sim 3$ –100 times smaller than those in the small EVN array. We made the exercise of producing an image with similar uv-range for both EVN and VLBA observations. The obtained uv-coverages result in the VLBA being sensitive to emission close to perpendicular to the structure we detected with the EVN (at an inclination  $\sim 50^\circ$ ), and since there is no emission in such orientation, the VLBA cannot detect any structure, unlike the EVN. Therefore, in order to better constrain the radio emission of NGC 6286, further VLBI observations covering proper hour angles at high sensitivity are needed.

## 4. X-RAY SPECTRAL ANALYSIS

The X-ray spectral analysis was performed within XSPEC v.12.8.2 (Arnaud 1996). Galactic absorption in the direction of the source ( $N_H^G = 1.8 \times 10^{20} \text{ cm}^{-2}$ , Kalberla et al. 2005) was taken into account by adding photoelectric absorption (TBABS in XSPEC, Wilms et al. 2000). Abundances were set to the solar value. Spectra were rebinned to have at least 20 counts per bin in order to use  $\chi^2$  statistics, unless reported otherwise.

In the following we first present the X-ray spectral analysis of the extended and nuclear emission revealed by *Chandra* (§ 4.1) and then discuss the spatially integrated broad-band X-ray emission (§ 4.2) considering all observations available.

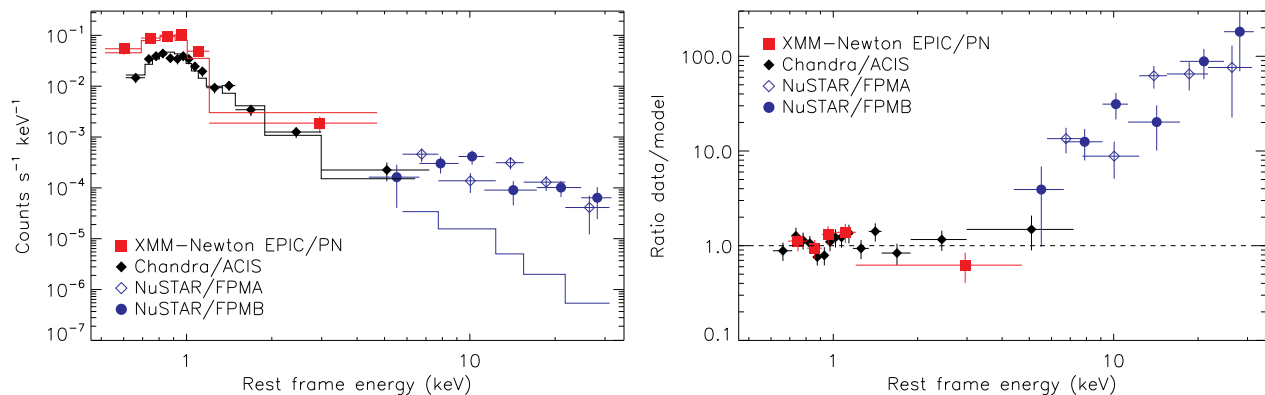


**Figure 4.** *Left panel:* *XMM-Newton* EPIC/PN, *Chandra* ACIS-S (using a 10.5 arcsec extraction radius) and *NuSTAR* FPMA/FPMB spectra of NGC 6286. The continuous lines represent the model used in Brightman & Nandra (2011) (APEC+ZPOWERLAW) to reproduce the 0.3–10 keV spectrum of the source. *Right panel:* ratio between the data and the model. The plots clearly show the importance of hard X-ray coverage to fully understand the characteristics of the X-ray emission.

#### 4.1. Extended and nuclear emission

The diffuse soft X-ray emission detected by *Chandra* has an angular size of  $\sim 12$  arcsec, which at the distance of the source corresponds to  $\sim 4.4$  kpc. This diffuse emission might either be related to thermal plasma in a star-forming region, to X-ray binaries, or to shocks created by the interaction between outflows from the AGN and the galactic medium. To analyse the diffuse and nuclear emission we extracted the spectra of the four regions shown in panel one of Fig. 2. Besides the 3–8 keV core, in order to study how the extended emission varies, we arbitrarily selected three regions (A, B and C) where most of the 0.2–2 keV photons were detected. Due to the low number of counts we rebinned the spectra to have at least 1 count per bin, and used Cash statistics (Cash 1979) to fit the data. In the following we discuss the spectral properties of the Core, and the regions A, B and C.

**Core.** The spectrum of the core was extracted from a circular region of radius 1.5 arcsec centred on the peak of the 3–8 keV emission. Ignoring the data below 1.2 keV to avoid contamination from the diffuse soft X-ray emission, and fitting with a power-law model (TBABS<sub>Gal</sub> × ZPOWERLAW in XSPEC) we obtain a photon index of  $\Gamma = -0.17^{+1.01}_{-1.03}$ . This low value is indicative of heavy absorption in the nuclear region. Fitting the X-ray spectrum using the whole energy range with a model that includes also a collisionally ionized plasma model (TBABS<sub>Gal</sub> × ZPOWERLAW + APEC) we obtain C-stat/DOF=20.9/21,  $\Gamma \leq -0.03$  and a plasma temperature of  $kT = 0.99^{+0.28}_{-0.35}$  keV. The 3–8 keV core coincides with the 1.4 GHz radio emission measured by the VLA FIRST survey (Becker et al. 1995).

**Region A.** Fitting the spectrum with a collisionally ionized thermal plasma model (TBABS<sub>Gal</sub> × APEC) results in a good fit (C-stat/DOF=31.0/37), with  $kT = 0.91^{+0.10}_{-0.18}$  keV. Applying a spectral model which reproduces a non-equilibrium plasma created in a shock (PSHOCK in XSPEC) yields C-stat/DOF=31.4/36, a plasma temperature of  $kT_s = 0.88^{+0.11}_{-0.13}$  keV and an upper limit on the ionization timescale of  $\tau_u \geq 1.6 \times 10^{12}$  s cm<sup>-3</sup>.

**Region B.** Using the thermal plasma model yields

a rather poor fit (C-stat/DOF=48.0/34). This can be improved by adding photoelectric absorption (TBABS<sub>Gal</sub> × ZTBABS × APEC, C-stat/DOF=43.7/33), and would be consistent with the presence of larger absorption in the central part of the edge-on galaxy with respect to other regions. The shock plasma model fails to reproduce well the spectrum both without (C-stat/DOF=48.7/33) and with (C-stat/DOF=43.6/32) an absorption component.

**Region C.** A thermal plasma model with  $kT = 1.23^{+0.37}_{-0.35}$  keV yields a good fit (C-stat/DOF=34/34), while a shock plasma model cannot reproduce well the data (C-stat/DOF=45.1/33), and results in  $kT_s = 1.09^{+0.73}_{-0.38}$  keV and  $\tau_u \leq 1.4 \times 10^8$  s cm<sup>-3</sup>.

#### 4.2. Spatially integrated X-ray emission

The *XMM-Newton* EPIC spectrum of NGC 6286 was analysed by Brightman & Nandra (2011), who found that it could be well represented by an unabsorbed power-law continuum plus a thermal plasma<sup>17</sup>, with the photon index fixed to  $\Gamma = 1.9$ . This is in disagreement with the hard ( $\Gamma = -0.17^{+1.01}_{-1.03}$ , see § 4.1) 1–8 keV spectrum of the 3–8 keV core. Fitting the *NuSTAR* FPMA/FPMB data with a simple power-law model we also find a very flat continuum ( $\Gamma = 0.49^{+0.46}_{-0.41}$ ). The low values of the photon index obtained in the 3–8 keV and 3–30 keV bands could indicate that the X-ray emission is highly absorbed.

While the model used by Brightman & Nandra (2011) can reproduce well the *XMM-Newton* and the spatially integrated *Chandra* spectra, it severely under predicts the hard X-ray flux inferred by *NuSTAR*, as illustrated in Fig. 4. This might be related either to heavy obscuration of the X-ray source or to flux variability between *XMM-Newton* and *NuSTAR* observations, although variability would not be able to explain the very flat hard X-ray spectrum. The *Swift*/XRT observation allows us to constrain the flux level below 10 keV band at the time of the *NuSTAR* observations. We find that the *Swift*/XRT 0.3–2 and 2–5 keV fluxes are consistent with that inferred by *Chandra* and *XMM-Newton* EPIC/PN observations (see Table 1), which implies the lack of significant variability

<sup>17</sup> ZPOWERLAW+APEC in XSPEC

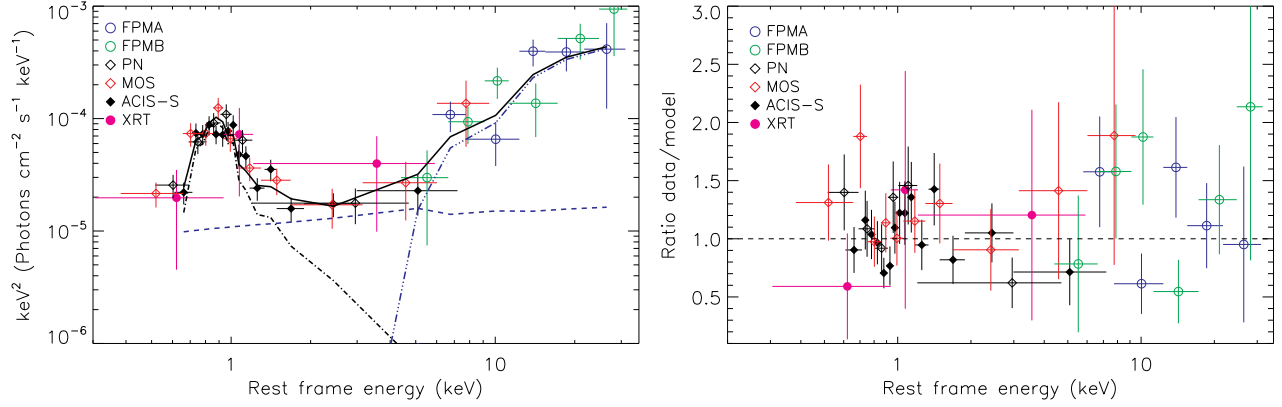


**Figure 5.** *Left panel:* unfolded broad-band X-ray spectrum of NGC 6286. The black continuous line represents the best fit to the data, while the dot-dashed line is the thermal plasma, the dashed line is the scattered emission and the dot-dot-dashed line is the SPHERE model. *Right panel:* ratio between the data and the model shown in the right panel.

**Table 1**  
Observed X-ray fluxes

| Facility          | Flux   |  |
|-------------------|--|--|
|                   | 0.3–2 keV<br>[ $10^{-14}$ erg s $^{-1}$ cm $^{-2}$ ] | 2–5 keV<br>[ $10^{-14}$ erg s $^{-1}$ cm $^{-2}$ ] |
| <i>Swift</i> /XRT | $8.4^{+4.1}_{-2.9}$                                  | $2.0^{+0.8}_{-1.0}$                                |
| <i>Chandra</i>    | $8.8^{+0.6}_{-0.6}$                                  | $2.0^{+0.3}_{-0.4}$                                |
| <i>XMM-Newton</i> | $9.5^{+0.8}_{-1.1}$                                  | $2.2^{+0.2}_{-0.4}$                                |

between the different observations. To further test the variability scenario we fitted *NuSTAR* and the spatially integrated *Chandra* spectra with a model that consists of a power-law plus a thermal plasma [TBABS<sub>Gal</sub> × (APEC + POWER LAW)], allowing for different normalisations of the power-law continuum to vary (fixing  $\Gamma = 1.9$ ). We found that the model cannot reproduce well the spectra ( $\chi^2/\text{DOF}=28.9/20$ ), with the fit<sup>18</sup> showing clear residuals between 10 and 30 keV. This rules out variability as a likely explanation for the large ratio between the 10–50 keV and 2–10 keV fluxes.

In the following we report the results obtained by adopting several different X-ray spectral models to infer the properties of the AGN in NGC 6286. In order to reduce the possible degeneracies in the models, we constrained the average properties of the diffuse soft X-ray emission. To do this we first extracted the *Chandra* X-ray spectrum of the diffuse emission by excluding from the circular region of 10.5 arcsec a circle of 1.5 arcsec centred on the 3–8 keV core. We then fitted the spectrum with a model that includes i) a thermal plasma and ii) a power-law component ( $\Gamma = 1.9$ ) to take into account the scattered emission. We obtained a normalization of the power law  $n_{\text{po}}^{\text{scatt}} = (1.03 \pm 0.37) \times 10^{-5}$  ph keV $^{-1}$  cm $^{-2}$  s $^{-1}$ , and a temperature and normalization of the thermal plasma of  $kT = 0.77^{+0.07}_{-0.08}$  keV and  $n_{\text{apc}} = (2.02 \pm 0.33) \times 10^{-5}$  ph keV $^{-1}$  cm $^{-2}$  s $^{-1}$ , respectively. In all the spectral models reported below we set  $n_{\text{po}}^{\text{scatt}}$ ,  $kT$  and  $n_{\text{apc}}$  to the values obtained for the dif-

fuse emission, and allow them to vary only within their 90% uncertainties.

#### 4.2.1. PEXRAV

To infer the value of the line-of-sight column density ( $N_{\text{H}}$ ) we fitted the joint *Swift*/XRT, *Chandra* ACIS-S, *XMM-Newton* EPIC/PN and MOS, and *NuSTAR* FPMA and FPMB data with a model that consists of: a) an absorbed power-law with a photon index fixed to  $\Gamma = 1.9$ , consistent with the average value of AGN (e.g., Nandra & Pounds 1994a; Piconcelli et al. 2005; Ricci et al. 2011), b) unabsorbed reprocessed X-ray emission from a slab, c) a Gaussian to reproduce the fluorescent Fe K $\alpha$  emission line (with the rest-frame energy fixed to  $E_{\text{K}\alpha} = 6.4$  keV), d) a second power-law to reproduce the scattered component, and e) emission from a collisionally ionized plasma. To reproduce the effect of obscuration we included both Compton scattering and photoelectric absorption. Reprocessed X-ray emission (excluding fluorescent lines) was taken into account using the PEXRAV model (Magdziarz & Zdziarski 1995). The fraction of scattered flux ( $f_{\text{scatt}}$ ) is calculated as the ratio between the normalization at 1 keV of the primary power law ( $n_{\text{po}}$ ) and  $n_{\text{po}}^{\text{scatt}}$ . The width of the Gaussian line was fixed to  $\sigma = 40$  eV, consistent with the results obtained by *Chandra*/HETG studies (e.g., Shu et al. 2010). An Fe K $\alpha$  line at 6.4 keV is usually found in the X-ray spectrum of AGN (e.g., Nandra & Pounds 1994b, Shu et al. 2010, Ricci et al. 2014b), and is believed to originate in the material surrounding the SMBH (e.g., Ricci et al. 2014a, Gandhi et al. 2015 and references therein). In XSPEC our model is:

$$\text{TBABS}_{\text{Gal}}(\text{ZTBABS} \times \text{CABS} \times \text{ZPOWERLAW} + \text{PEXRAV} + \text{ZGAUSS} + \text{APEC} + \text{ZPOWERLAW}).$$

The model yields a good fit ( $\chi^2/\text{DOF}=47.2/44$ ) and results in a column density consistent with borderline Compton-thick obscuration ( $N_{\text{H}} = 1.32^{+0.82}_{-0.54} \times 10^{24}$  cm $^{-2}$ ). Due to the low signal-to-noise ratio, the Fe K $\alpha$  is not spectrally resolved, and only an upper limit of its equivalent width was obtained ( $EW \leq 2318$  eV), which is consistent with heavy obscuration.

#### 4.2.2. TORUS

To further study the absorbing material we used the TORUS model developed by Brightman & Nandra (2011),

<sup>18</sup> the ratio of the power-law normalisations is  $\simeq 4$ .



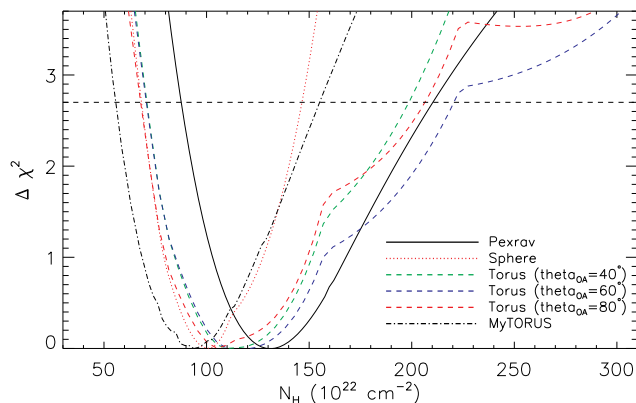


**Figure 6.** Value of  $\Delta\chi^2 = \chi^2 - \chi_{\text{best}}^2$  (where  $\chi_{\text{best}}^2$  is the minimum value of the  $\chi^2$ ) versus the column density for the different X-ray spectral models discussed in §4.2. The horizontal dashed line represents  $\Delta\chi^2 = 2.7$ . The plot shows that NGC 6286 is heavily obscured, with  $N_{\text{H}}$  consistent with the source being CT for the five models considered.

which considers reprocessed and absorbed X-ray emission from a spherical-toroidal structure. In this model the line-of-sight column density is independent of the inclination angle, which we fixed to the maximum value permitted ( $\theta_i = 87.1^\circ$ ). Similarly to what was done for PEXRAV, we added to the model a power law, to take into account the scattered emission, and a collisionally ionized plasma model. In XSPEC, the model is

$$\text{TBABS}_{\text{Gal}}(\text{ATABLE}\{\text{TORUS1006.FITS}\} + \text{APEC} + \text{ZPOWERLAW}).$$

We fixed  $\Gamma = 1.9$  and tested several values of the half-opening angle of the torus ( $\theta_{\text{OA}} = 40^\circ, 60^\circ, 80^\circ$ ). The three models are statistically indistinguishable, and in all cases we obtained good fits. For the three values of  $\theta_{\text{OA}}$  the column densities are consistent within the uncertainties with CT absorption.

#### 4.2.3. SPHERE

To test the scenario in which the X-ray source is fully covered by the obscuring material we applied the SPHERE model (Brightman & Nandra 2011), using the same setting as for the TORUS model:

$$\text{TBABS}_{\text{Gal}}(\text{ATABLE}\{\text{SPHERE0708.FITS}\} + \text{APEC} + \text{ZPOWERLAW}).$$

This model provides a good fit (Fig. 5), and confirms the presence of heavy obscuration ( $N_{\text{H}} = 9.8_{-3.5}^{+4.6} \times 10^{23} \text{ cm}^{-2}$ ).

#### 4.2.4. MYTORUS

Next we applied the MYTORUS model (Murphy & Yaqoob 2009), which considers absorbed and reprocessed X-ray emission from a smooth torus with  $\theta_{\text{OA}} = 60^\circ$ , and can be used for spectral fitting as a combination of three additive and exponential table models: the zeroth-order continuum (MYTORUSZ), the scattered continuum (MYTORUSS) and a component containing the fluorescent emission lines (MYTORUSL). We used the *decoupled* version of MYTORUS (Yaqoob 2012). This was done by: i) allowing the values of the column density of the absorbing [ $N_{\text{H}}^{\text{T}}(Z)$ ] and reprocessing [ $N_{\text{H}}^{\text{T}}(S, L)$ ] material to have different

values; ii) fixing the inclination angle of MYTORUSL and MYTORUSS to  $\theta_i(S, L) = 0^\circ$ , and that of MYTORUSZ to  $\theta_i(Z) = 90^\circ$ ; iii) adding a second scattered component with  $\theta_i(S, L) = 90^\circ$ ; iv) leaving the normalizations of the transmitted and scattered component ( $n_{\text{po}}$  and  $n_{\text{refl}}$ ) free to vary. To this model we added a scattered component and thermal emission. In XSPEC the model is:

$$\text{TBABS}_{\text{Gal}} \times \{ \text{MYTORUSZ}(90^\circ) \times \text{ZPOWERLAW} + \text{MYTORUSS}(0^\circ) + \text{MYTORUSS}(90^\circ) + \text{GSMOOTH}[\text{MYTORUSL}(0^\circ) + \text{MYTORUSL}(90^\circ)] + \text{APEC} + \text{ZPOWERLAW} \}.$$

Due to the low signal-to-noise ratio of the spectrum we could not constrain the different values of  $N_{\text{H}}^{\text{T}}(S, L)$  and  $N_{\text{H}}^{\text{T}}(Z)$ , so their values were tied. The same was done for the normalizations of the scattered and transmitted components, while the photon index was left free to vary. This model also yields a good fit and results in a line-of-sight column density consistent with heavy obscuration ( $N_{\text{H}} = 8.8_{-3.8}^{+5.1} \times 10^{23} \text{ cm}^{-2}$ ).

The parameters obtained from the spectral analysis are reported in Table 3, while in Figure 6 we show the values of  $\Delta\chi^2$  versus  $N_{\text{H}}$  for the models described above. Depending on the X-ray spectral model adopted, the intrinsic (i.e. absorption and k-corrected) 2–10 keV luminosity of NGC 6286 is  $3 - 20 \times 10^{41} \text{ erg s}^{-1}$ .

## 5. DISCUSSION

The X-ray spectral analysis of NGC 6286 reported above clearly shows that the accreting SMBH is heavily obscured, possibly by CT material (see Fig. 6). The very flat continuum found by both *Chandra* (for the hard X-ray core) and *NuSTAR*, together with the fact that the 1.4 GHz emission coincides with the 3–8 keV *Chandra* point-source (Panel 2 of Fig. 2) confirms the presence of a heavily obscured AGN. While the buried AGN in NGC 6286 could be easily identified at hard X-rays, several other diagnostics failed to detect it because of its low-luminosity. In §5.1 we illustrate the most commonly adopted techniques to detect AGN in U/LIRGs, and discuss the case of NGC 6286 by exploiting the wealth of multi-wavelength data available for the GOALS sample. In §5.2 we estimate the contribution of the AGN to the luminosity of NGC 6286, while in §5.3 we discuss the optical and radio properties of the galaxy, comparing them to those of other similar LIRGs. Finally, in §5.4, we discuss the presence of heavily obscured low-luminosity AGN in LIRGs.

### 5.1. IR and X-ray tracers of AGN activity in U/LIRGs

AGN in U/LIRGs can be identified in the IR by several means: i) with the detection of high-excitation MIR emission lines (e.g., Sturm et al. 2002), and in particular of [Ne V] 14.32  $\mu\text{m}$  and [Ne V] 24.32  $\mu\text{m}$  (e.g., Weedman et al. 2005, Satyapal et al. 2008, Goulding & Alexander 2009); ii) using the ratios of high-to-low ionization fine-structure emission lines (e.g., [Ne V] 14.32  $\mu\text{m}$ /[Ne II] 12.8  $\mu\text{m}$  and [O IV] 25.89  $\mu\text{m}$ /[Ne II] 12.8  $\mu\text{m}$ ; e.g., Lutz et al. 1999, Petric et al. 2011); iii) with the EW of the PAH features, which tend to be lower in the presence of a

**Table 2**  
List of IR and X-ray tracers of AGN activity commonly used for U/LIRGs.

| (1)<br>Indicator   | (2)<br>NGC 6286  | (3)<br>Reference        | (4)<br>Mean GOALS                    | (5)<br>Threshold | (6)<br>AGN |
|--|------------------|-------------------------|--------------------------------------|------------------|------------|
| [Ne V] 14.32 $\mu$ m [ $10^{-17}$ W m $^{-2}$ ]            | $0.33 \pm 0.11$  | Dudik et al. (2009)     | 2.27 <sup>A</sup>                    | ...              | ?          |
| [Ne V] 24.32 $\mu$ m [ $10^{-17}$ W m $^{-2}$ ]            | $0.99 \pm 0.20$  | Dudik et al. (2009)     | ...                                  | ...              | ?          |
| [Ne V]/[Ne II]   | 0.02             | Dudik et al. (2009)     | 0.07 <sup>B</sup>                    | $\geq 0.1^C$     | ×          |
| [OIV]/[Ne II]  | 0.05             | Dudik et al. (2009)     | 0.03 <sup>D</sup> /0.24 <sup>E</sup> | $\geq 1.75^F$    | ×          |
| $\Gamma_{2.5-5\mu\text{m}}$                                | -0.1             | Imanishi et al. (2010b) | ...                                  | $\geq 1^G$       | ×          |
| $F_\nu(30\mu\text{m})/F_\nu(15\mu\text{m})$                | 5.97             | Stierwalt et al. (2013) | $8^{+2}_{-1.5}^H$                    | ...              | ×          |
| $EW(\text{PAH } 3.3\mu\text{m})[\text{nm}]$                | 48               | Imanishi et al. (2010b) | ...                                  | $< 40^G$         | ×          |
| $EW(\text{PAH } 6.2\mu\text{m}) [\mu\text{m}]$             | 0.59             | Stierwalt et al. (2013) | 0.55 <sup>H</sup>                    | $\leq 0.3^C$     | ×          |
| $\tau_{3.1\mu\text{m}}$ (3.1 $\mu$ m H <sub>2</sub> O ice) | ND               | Imanishi et al. (2010b) | ...                                  | $> 0.3^G$        | ×          |
| $\tau_{3.4\mu\text{m}}$ (3.4 $\mu$ m bare carbonaceous)    | ND               | Imanishi et al. (2010b) | ...                                  | $> 0.2^G$        | ×          |
| $\tau_{9.7\mu\text{m}}$                                    | -0.40            | Stierwalt et al. (2013) | -0.35 <sup>H</sup>                   | ...              | ×          |
| <i>Chandra</i> hardness ratio                              | $-0.85 \pm 0.07$ | This work               | -0.56 <sup>I</sup>                   | $> -0.3^J$       | ×          |
| Observed log $L_{2-10}$ [erg s $^{-1}$ ]                   | 40.80            | This work               | 41.3 <sup>K</sup>                    | $> 42^L$         | ×          |
| Radio/FIR flux ratio ( $q$ )                               | 2                | U et al. (2012)         | $2.41 \pm 0.29^M$                    | $< 1.64^N$       | ×          |

The table lists (1) the indicator used, (2) the value and (3) reference for NGC 6286, (4) the mean value for the GOALS sample, (5) the threshold used to infer the presence of AGN, and (6) whether an AGN was found or not.

**Notes.** ND: not detected; <sup>A</sup> median of the 43 detections (18% of the sample) from Petric et al. (2011); <sup>B</sup> median (Petric et al. 2011); <sup>C</sup> threshold used by Inami et al. (2013) to establish a significant contribution of the AGN to the MIR flux. <sup>D</sup> median and <sup>E</sup> mean from Petric et al. (2011); <sup>F</sup> Value indicating if the AGN contributes to more than 50% of the MIR flux (Petric et al. 2011); <sup>G</sup> value used by Imanishi et al. (2010b) <sup>H</sup> mean value for objects in the same merger stage (B) as NGC 6286 (Stierwalt et al. 2013), the 30 $\mu$ m/15 $\mu$ m flux density ratio of NGC 6286 is only marginally lower than the average value for the B merger stage, and has a value consistent with 63% of GOALS LIRGs; <sup>I</sup> median of the 44 objects reported in Iwasawa et al. (2011); <sup>J</sup> value used to establish the presence of an AGN and <sup>K</sup> median value (Iwasawa et al. 2011); <sup>L</sup> Values commonly used to separate AGN from starbursts in the 2–10 keV band (e.g., Szokoly et al. 2004, Kartaltepe et al. 2010); <sup>M</sup> mean obtained for the 64 objects studied by U et al. (2012); <sup>N</sup> threshold for radio-excess defined by Yun et al. (2001).

bright AGN, since it can destroy PAH molecules (e.g., Imanishi et al. 2010b); iv) studying the slope of the 2.5–5 $\mu$ m continuum ( $\Gamma_{2.5-5}$ , e.g., Imanishi et al. 2010b) or the continuum 30 $\mu$ m/15 $\mu$ m flux density ratio (e.g., Stierwalt et al. 2013), which tend to be red in the presence of an AGN; v) using the depth of absorption features (e.g., Imanishi & Dudley 2000; Risaliti et al. 2006; Georgantopoulos et al. 2011b), with large depths pointing towards AGN obscured by dust; and/or vi) from deviations of the well known correlation between the far-IR (FIR) and the radio luminosity (Helou et al. 1985, Condon et al. 1991, Condon 1992), using the radio-FIR flux ratio  $q$  (e.g., Yun et al. 2001). We find that all these proxies (Table 2) fail to detect the AGN in NGC 6286, with the exception of the Ne V lines. These lines can however also be produced by a young starburst with a large population of Wolf-Rayet and O stars (e.g., Abel & Satyapal 2008), so their detection does not always provide conclusive evidence of an AGN. This is especially true for NGC 6286, since the Ne V lines are weak [ $\log(L_{[\text{Ne V}]}/\text{erg s}^{-1}) \sim 38.8$ ]. Moreover, the detection of the [Ne V] lines has been questioned by Inami et al. (2013), who found [Ne V] 14.32 $\mu$ m to be detected only in one of the two *Spitzer* observations available, while in both observations a feature possibly consistent with [Ne V] 24.32 $\mu$ m were

detected at  $\sim 24.37\mu\text{m}$  (Inami, private communication). *Spitzer*/IRAC selection provides another important tool for identifying AGN (e.g., Lacy et al. 2004, Stern et al. 2005). Using the AGN selection criteria proposed by Donley et al. (2012) (see Eq. 1 and 2 in their paper), and considering the fluxes reported by U et al. (2012), we find that NGC 6286 does not satisfy the conditions for the presence of an AGN. The fact that the IR proxies fail to identify the AGN emission in NGC 6286 is due to the problematic identification of low-luminosity AGN with IR spectra dominated by the host. For example, in a low-luminosity AGN the silicate absorption feature would be diluted by the strong IR continuum of the host galaxy.

Iwasawa et al. (2011) studied 44 LIRGs from the GOALS sample with *Chandra*, and assessed the presence of an AGN using the hardness ratio  $HR \equiv (H - S)/(H + S)$ , where  $H$  and  $S$  are the background-corrected counts in the 2–8 and 0.5–2 keV ranges, respectively. Sources with  $HR > -0.3$  are reported as candidate AGN. This value was chosen because ULIRGs which are known to host AGNs, such as Mrk 231, Mrk 273, and UGC 5101, tend to cluster just above this limit (Iwasawa et al. 2009). Considering the spatially-integrated X-ray flux NGC 6286 has a hardness ratio  $HR = -0.85 \pm 0.07$ , which would not allow to infer the presence of an AGN. However, as discussed by Iwasawa et al. (2011)



this threshold could become less reliable for some CT AGN, since mostly reprocessed radiation is observed in the hard X-ray band. Another criteria commonly used to identify AGN is the observed 2–10 keV X-ray luminosity. Using  $\log(L_{2-10}/\text{erg s}^{-1}) > 42$  as a threshold (e.g., Szokoly et al. 2004, Kartaltepe et al. 2010), one would also miss identifying NGC 6286 as a buried AGN [ $\log(L_{2-10}/\text{erg s}^{-1}) = 40.80$ ].

Spectral decomposition (e.g., Nardini et al. 2008, Alonso-Herrero et al. 2012) is another powerful method to constrain the contribution of AGN to the multi-wavelength SED. Vega et al. (2008) found that a pure starburst model fails to reproduce well the near-IR to radio SED of NGC 6286, and a buried AGN accounting for 5% of the IR luminosity is required by the data. An useful diagnostic of the presence of a heavily obscured AGN is the ratio between the MIR and the 2–10 keV luminosities (e.g., Alexander et al. 2008; Rovilos et al. 2014; Georgantopoulos et al. 2011a). It has been shown indeed that for AGN the absorption-corrected 2–10 keV and the 6 and 12  $\mu\text{m}$  luminosities are well correlated (e.g., Gandhi et al. 2009; Stern 2015; Asmus et al. 2015), so that deviations from the correlation might imply the presence of heavy obscuration. Vega et al. (2008) report that at 6  $\mu\text{m}$  about 58% of the flux is produced by the AGN. This would imply that the ratio between the IR and observed X-ray AGN luminosity is very low:  $L_{2-10}/L_{6\mu\text{m}} \simeq 2.4 \times 10^{-3}$ . This value is consistent with undetected DOGs in the CDF-N (Georgakakis et al. 2010) and with other U/LIRGs (Georgantopoulos et al. 2011a), which is related to the fact that in U/LIRGs the IR emission is enhanced by strong star formation, leading to very low values of  $L_{2-10}/L_{6\mu\text{m}}$ . Using the largest 2–10 keV X-ray luminosity obtained in § 4 ( $L_{2-10} \sim 2 \times 10^{42} \text{ erg s}^{-1}$ ) one would still find that  $L_{2-10}/L_{6\mu\text{m}} \sim 0.1$ , a value lower than that expected from the  $L_{2-10} - L_{6\mu\text{m}}$  correlation. This might imply that the AGN contribution to the IR flux is significantly lower than that reported by Vega et al. (2008) (see § 5.2 and Fig. 7).

### 5.2. AGN contribution to the IR luminosity

The IR luminosity of NGC 6286 is  $8.8 \times 10^{44} \text{ erg s}^{-1}$ , which would imply that, depending on the X-ray spectral model used, we obtain a ratio  $L_{2-10}/L_{\text{IR}} \simeq 4 \times 10^{-4} - 2.3 \times 10^{-3}$ , significantly lower than the value expected from pure AGN (e.g., Mullaney et al. 2011). Considering the observed 2–10 keV luminosity, the ratio is  $\log(L_{2-10}^{\text{obs}}/L_{\text{IR}}) \simeq -4.14$ , which is consistent with the average value found for the GOALS sample [ $\log(L_{2-10}^{\text{obs}}/L_{\text{IR}}) = -4.40 \pm 0.63$ , Iwasawa et al. 2011].

Using the relationship of Mullaney et al. (2011), it is possible to convert the 2–10 keV luminosity into the expected IR luminosity emitted by the dust around the AGN:

$$\log L_{\text{IR},43}^{\text{AGN}} = (0.53 \pm 0.26) + (1.11 \pm 0.07) \log L_{2-10,43}. \quad (1)$$

In the above equation  $L_{\text{IR},43}^{\text{AGN}}$  and  $L_{2-10,43}$  are the 8–1000  $\mu\text{m}$  and 2–10 keV luminosities of the AGN in units of  $10^{43} \text{ erg s}^{-1}$ . Considering the range of values obtained for the 2–10 keV intrinsic luminosity, the IR luminosity of the AGN is  $\log(L_{\text{IR}}^{\text{AGN}}/\text{erg s}^{-1}) = 41.91 - 42.75$ .

Comparing this to the IR luminosity of the system [ $\log(L_{\text{IR}}/\text{erg s}^{-1}) = 44.96$ ] we find that the IR luminosity of the AGN is between 0.1 and 0.6% of the total IR luminosity. This value is in disagreement with that obtained by Vega et al. (2008) using spectral decomposition, who found that the contribution of the AGN to the total IR luminosity is about one order of magnitude larger. A 5% contribution to the total IR luminosity would imply that  $\log(L_{\text{IR}}^{\text{AGN}}/\text{erg s}^{-1}) = 43.66$  and the intrinsic 2–10 keV luminosity of the AGN would be  $\log(L_{2-10}/\text{erg s}^{-1}) = 43.12$ , also an order of magnitude larger than predicted by our X-ray spectral analysis. To have such a luminosity, the AGN should be obscured by  $\log(N_{\text{H}}/\text{cm}^{-2}) > 25$ , which is inconsistent with the results obtained here. An alternative explanation for this discrepancy is that the AGN is intrinsically weak at X-ray wavelengths, as recently found by *NuSTAR* for the AGN in Mrk 231 (Teng et al. 2014, see also Teng et al. 2015).

Assuming a 2–10 keV bolometric correction of  $\kappa_x = 20$  (e.g., Vasudevan & Fabian 2007), the bolometric output of the AGN would be  $7 - 40 \times 10^{42} \text{ erg s}^{-1}$ . This implies that the ratio between the IR luminosity and the total output of the AGN is  $L_{\text{AGN}}^{\text{Bol}}/L_{\text{IR}} \simeq 0.8 - 4.5\%$ . The AGN bolometric output can also be inferred from the [Ne V] 14.32  $\mu\text{m}$  luminosity, following the relation obtained by Satyapal et al. (2007):

$$\log L_{\text{Bol}}^{\text{AGN}} = 0.938 \log L_{[\text{Ne V}]} + 6.317, \quad (2)$$

and is  $\log(L_{\text{Bol}}^{\text{AGN}}/\text{erg s}^{-1}) \sim 42.7$ , consistent with the estimate obtained using the X-ray luminosity. The 2–10 keV bolometric correction obtained using this value is  $\kappa_x \simeq 3 - 17$ . The black hole mass of NGC 6286 has been estimated to be  $M_{\text{BH}} \sim 2.7 \times 10^8 M_{\odot}$  by Caramete & Biermann (2010) using the black hole mass-spheroid correlation (e.g., Magorrian et al. 1998). The Eddington ratio of the source would then be  $\lambda_{\text{Edd}} \simeq (0.2 - 1.2) \times 10^{-3}$ , consistent with a low accretion rate AGN.

The lack of a significant AGN contribution to the total IR flux is also confirmed considering the [Ne V]/[Ne II] ratio versus the EW of the 6.2  $\mu\text{m}$  PAH feature [see Fig. 1 and 2 of Petric et al. (2011)], which shows that the ratio between  $L_{\text{IR}}^{\text{AGN}}$  and  $L_{\text{IR}}$  is below 1% for this object. This, together with the 2–10 keV bolometric correction obtained using [Ne V] 14.32  $\mu\text{m}$ , clearly disfavours the intrinsically X-ray weak AGN scenario. We can therefore conclude that the energetics of NGC 6286 are clearly dominated by the host galaxy, with the low-luminosity AGN providing only a minor contribution to the total flux. The contribution of the AGN to the IR flux of the system is shown in Fig. 7.

### 5.3. Optical and radio emission

NGC 6286 has been classified as a low-ionization nuclear emission-line region (LINER) by Veilleux & Osterbrock (1987) using a classification scheme based on the diagram first proposed by Baldwin, Phillips & Terlevich (1981). While most LINERs appear to be driven by old stellar populations (e.g., Sarzi et al. 2010) and by shocks in ULIRGs (e.g., Soto & Martin 2010, 2012), in some cases they can be associated to low-luminosity AGN (e.g., Ho 2008). Yuan et al.

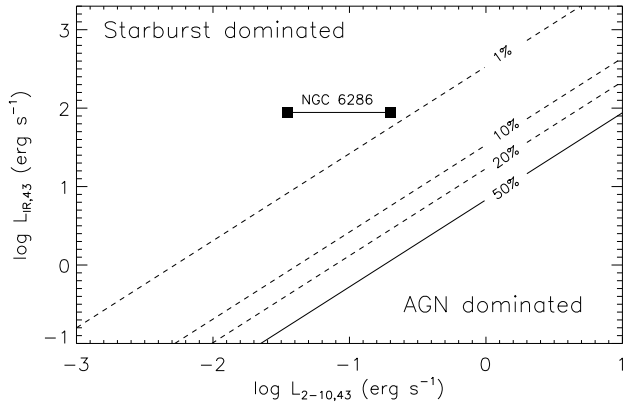


**Figure 7.** Intrinsic X-ray luminosity of the AGN in the 2–10 keV band versus the total IR luminosity of the system (in the 8–1000 $\mu$ m band). Both luminosities are in units of  $10^{43}$  erg s $^{-1}$ . The continuous black line represents the values for which AGN and starburst contribute in the same amount to the IR flux, while the dashed lines show contributions of the AGN of 20, 10 and 1%. The values of the IR luminosity expected to be due to the AGN are calculated from the 2–10 keV luminosity following Eq. 1. The two values of the 2–10 keV luminosity of NGC 6286 represent the minimum and maximum value obtained with the different models discussed in Sect 4.2 (see also Table 3). The figure shows that the AGN in NGC 6286 contributes  $< 1\%$  of the total IR luminosity.

(2010) have recently used a new semi-empirical optical spectral classification to classify IR-selected galaxies based on three diagrams: [OIII]/H $\beta$  versus [NII]/H $\alpha$ , [SII]/H $\alpha$  and [OI]/H $\alpha$  line ratios. This is based on the work of Kewley et al. (2006) to separate starburst galaxies, starburst/AGN composite galaxies, Seyfert 2s, and LINERs. In the scheme of Kewley et al. (2006) objects that were classified as LINERs according to Veilleux & Osterbrock (1987) would be either true LINERs, Seyfert 2s, composite HII-AGN galaxies, or high metallicity star-forming galaxies. Yuan et al. (2010) found that true LINERs are rare in IR-selected samples ( $< 5\%$ ), and most of the objects would be either classified as star-forming galaxies or starburst/AGN composites. Yuan et al. (2010) classified NGC 6286 as a composite using [NII], a HII region using [SII] and a LINER using [OI]. Therefore they adopted a composite classification for the source, which might imply the presence of an AGN. Yuan et al. (2010) found that in the IR luminosity bin  $L_{\text{IR}} = 10^{11} - 10^{12} L_{\odot}$  about 37% of the objects in the *IRAS* Bright Galaxy Sample (BGS, Sanders et al. 1995, Veilleux et al. 1995) are classified as composites.

To characterise the relative AGN contribution to the extreme ultraviolet (EUV) radiation field, Yuan et al. (2010) use  $D_{\text{AGN}}$ , which is the normalised distance from the outer boundary of the star-forming sequence. While this quantity does not provide information on the fraction of emission due to the AGN, it can be used to compare the amount of EUV radiation due to the AGN in different objects. For NGC 6286 they found  $D_{\text{AGN}} = 0.5$  using both the [OI]/H $\alpha$  and the [NII]/H $\alpha$  diagram. Yuan et al. (2010) found a statistically significant increase of  $D_{\text{AGN}}$  with  $L_{\text{IR}}$ , consistent with the idea that the fraction of AGN increases for increasing values of the 8–100 $\mu$ m luminosity (e.g., Veilleux et al. 1995). The value obtained for NGC 6286 is marginally larger than the average value obtained by Yuan et al. (2010) for the

BGS sample for  $11 < \log(L_{\text{IR}}/L_{\odot}) < 12$  ( $D_{\text{AGN}} \simeq 0.35$ ).

The dense molecular gas tracer HCN has been found to be enhanced (relative to HCO $^{+}$  and CO) in systems with dominant AGN (e.g., Imanishi et al. 2007). Privon et al. (2015) have shown that some pure starburst and composite sources show similarly enhanced HCN emission. The origin of this enhancement is uncertain, but might be due to mid-infrared pumping associated with a compact obscured nucleus (CON; e.g., Aalto et al. 2015). However, the HCN/HCO $^{+}$  ratio of NGC 6286 is consistent with that of normal starbursts, rather than CONs. From this we can conclude that the starburst does not appear to be compact.

A radio core is rather common in low-luminosity AGN, as shown by the work of Nagar et al. (2005), who found evidence of radio emission in  $\geq 50\%$  of the low-luminosity AGN of the Palomar Spectroscopic sample (see also Ho 2008). The flux of NGC 6286 at 1.4 GHz is  $f_{1.4\text{ GHz}} = 157.4 \pm 5.6$  mJy (Condon et al. 1998), which implies that the radio loudness is  $\log R_X = \log(f_{1.4\text{ GHz}}/f_{2-10}) = -2.6$  to  $-3.1$ , depending on the X-ray spectral model assumed. These values were obtained taking into account only the nuclear emission in the computation of the 2–10 keV flux. Considering the threshold suggested by La Franca et al. (2010) (see also Panessa et al. 2007, Terashima & Wilson 2003),  $\log R_X = -4.3$ , NGC 6286 would be classified as radio-loud AGN. Murphy (2013) report that the radio spectral index<sup>19</sup> of NGC 6286 is  $\alpha_{\text{low}} = -0.73 \pm 0.03$ ,  $\alpha_{\text{mid}} = -0.89 \pm 0.03$  and  $\alpha_{\text{high}} = -1.02 \pm 0.12$  for  $\nu < 5$  GHz,  $1 < \nu/\text{GHz} < 10$  and  $\nu > 10$  GHz, respectively. This would point towards a significant contribution of synchrotron emission, possibly from a jet. The two radio sources detected by EVN and coincident with the 3–8 keV core could be in fact associated to a jet and counter jet, consistent with the radio-loud classification of NGC 6286.

#### 5.4. Heavily obscured low-luminosity AGN in U/LIRGs

As discussed above for the case of NGC 6286, the identification of heavily obscured AGN in LIRGs can be rather difficult if the AGN has a low-luminosity. The EW of PAH features would not be significantly affected by the AGN if it is highly obscured, since the gas and dust would shield the PAH-emitting molecules, or if it is not very luminous. A low-luminosity AGN would also be difficult to find by studying the 2.5–5 $\mu$ m slope, since the IR emission would be dominated by the starburst, and the AGN emission can still be self-absorbed. Absorption features also would not be able to help if the AGN is not very luminous. A more reliable tracer is [Ne V], but while its detection might indicate the presence of an AGN, its non-detection does not exclude it. Moreover, [Ne V] could be created in young starbursts, and for low-luminosity AGN it could be too faint to be detected (see Eq. 2). Radio studies can also give important insights, but since not all AGN are very strong at these wavelengths, results are not always conclusive. Hard X-ray studies are possibly the best way to unveil obscured AGN in U/LIRGs, although they can also be limited by absorption for  $\log(N_{\text{H}}/\text{cm}^{-2}) \gg 24$ .

<sup>19</sup> We consider here the following definition of the spectral index:  $F_{\nu} \propto \nu^{\alpha}$ .

By using multi-wavelength indicators of AGN for a subsample of 53 U/LIRGs within the GOALS sample, U et al. (2012) found that  $\sim 60\%$  and  $\sim 25\%$  of ULIRGs and LIRGs host AGN. Studying the whole GOALS sample, Petric et al. (2011) found that 18% of the LIRGs show evidence of [Ne V]  $14.32\mu\text{m}$ , and hence might host an AGN. By means of optical spectroscopy, Yuan et al. (2010) found that 59% of the 51 single nuclei galaxies with  $11 < \log(L_{\text{IR}}/L_{\odot}) < 12$  in the BGS sample host an AGN<sup>20</sup>. The fraction of AGN is larger (77%) if one considers only two of the three diagrams for the spectral classification. A significant fraction of the composite systems might hide buried low-luminosity AGN, as in the case of NGC 6286, although an important contribution to the line emission in these objects might be due to shocks (e.g., Soto et al. 2012). Treister et al. (2010b) have shown, by stacking *Chandra* spectra of LIRGs in the *Chandra* Deep Field-South, that 15% of the objects with  $L_{\text{IR}} > 10^{11} L_{\odot}$  contain heavily obscured AGN. By stacking X-ray spectra in different bins of stellar mass, they found a significant excess at  $E = 6 - 7 \text{ keV}$  in the stacked spectrum of sources with mass  $M > 10^{11} M_{\odot}$ , very likely related to a prominent Fe K $\alpha$  line, while no clear evidence of AGN activity was found in less-massive galaxies. Treister et al. (2010b) concluded that there might be a large population of heavily obscured AGN in high mass galaxies. NGC 6286, with a stellar mass of  $1.26 \times 10^{11} M_{\odot}$  (Howell et al. 2010), fits extremely well into this scenario in the local Universe.

We have shown in § 5.1 and 5.3 that NGC 6286 has optical and IR characteristics quite typical of LIRGs, and consistent with other galaxies of the GOALS sample for the same merger stage. It is interesting to notice that also the hardness ratio and the observed 2–10 keV luminosity inferred by *Chandra* are consistent with a large fraction of the objects of the sample of Iwasawa et al. (2011) (see Fig. 5 and 6 of their paper, respectively), which might indicate that several more heavily obscured low-luminosity AGN are present in LIRGs of the GOALS sample. Moreover, we have shown that in the low-count regime it is possible to miss obscured AGN by adopting a simple phenomenological model to reproduce their X-ray spectra. Therefore there might be a significant population of low-luminosity heavily obscured AGN in LIRGs that we are missing due to the lack of sensitive hard X-ray observations. Numerical simulations have shown that accretion onto SMBHs might be happen at some level even after the first encounter (e.g., Di Matteo et al. 2005), although the expected accretion rate varies depending on the galaxy mergers code adopted (e.g., Gabor et al. 2015). Our on-going campaign of *NuSTAR* observations of ten LIRGs will allow us to study the AGN fraction in merging galaxies in the hard X-ray band across the whole merger sequence.

Another object showing similar characteristics to NGC 6286 is IC 883, a LIRG in a late merger stage that was found to host a low-luminosity AGN from radio observations (Romero-Cañizales et al. 2012b; Romero-Cañizales et al., in prep.). As for NGC 6286, the IR emission of IC 883 is dominated by star-formation and the AGN does not contribute significantly to the ener-

getics of the system. Interestingly, similar to NGC 6268, IC 883 is also reported as a composite AGN/starburst system by Yuan et al. (2010), along with more than one third of LIRGs from the BGS sample.

## 6. SUMMARY AND CONCLUSIONS

We have reported here the first results of a *NuSTAR* campaign aimed at observing ten LIRGs in different merger stages, focussing on the first detection of a heavily obscured AGN in NGC 6286. The *Chandra*/ACIS-S 0.3–2 keV image of the source shows extended emission that covers  $\sim 4.4 \text{ kpc}$  (Fig. 2), and which might be due to collisionally ionized plasma. In the 3–8 keV band we found a compact source, with a flat 1.2–8 keV spectrum ( $\Gamma \sim -0.2$ ), which coincides with the radio emission detected by FIRST. The *NuSTAR* spectrum also shows a flat X-ray continuum ( $\Gamma \sim 0.5$ ). By analysing the broad-band X-ray spectrum of the source, combining archival *XMM-Newton*, *Chandra* and quasi-simultaneous *NuSTAR* and *Swift*/XRT observations, we have found that the source is consistent with being obscured by mildly CT material ( $N_{\text{H}} = 1.08^{+0.63}_{-0.38} \times 10^{24} \text{ cm}^{-2}$ , Fig. 6). The presence of a heavily obscured AGN is confirmed by the possible detection of weak [Ne V]  $14.32\mu\text{m}$  and [Ne V]  $24.32\mu\text{m}$  lines (Dudik et al. 2009), by near-IR to radio spectral decomposition (Vega et al. 2008) and by the optical classification of the galaxy as an AGN/starburst composite (Yuan et al. 2010).

The buried AGN has an intrinsically low luminosity ( $L_{2-10} \sim 3 - 20 \times 10^{41} \text{ erg s}^{-1}$ ), a low value of the Eddington ratio [ $\lambda_{\text{Edd}} \simeq (0.2 - 1.2) \times 10^{-3}$ ] and seems to contribute less than 1% to the energetics of the system (Fig. 7). Because of its low luminosity, previous observations carried out below 10 keV and in the infrared did not notice the presence of a buried AGN. By exploiting the rich multi-wavelength coverage of U/LIRGs in the GOALS sample we have discussed the radio to X-ray characteristics of NGC 6286, showing that they are consistent with those of objects with similar luminosities and in a similar merger stage. We speculated that there might be a significant fraction of low-luminosity AGN in LIRGs that we are missing due to their low contribution to the total IR flux of the system. In particular, more than one third of LIRGs from the BGS sample are classified as composite AGN/starburst system by Yuan et al. (2010), and might hide low-luminosity highly obscured AGN.

The case of NGC 6286 clearly shows the importance of hard X-ray coverage in order to detect low-luminosity heavily obscured AGN in LIRGs. Our ongoing *NuSTAR* campaign of LIRGs will put better constraints on the fraction of these objects and the relation between obscured accretion and merger stage.

We thank the anonymous referee for his/her comments, that helped us to improve the quality of our manuscript, and the *NuSTAR* Cycle 1 TAC for the *NuSTAR* data on which this paper is based. CR acknowledges C.S. Chang, H. Inami, P. Gandhi and S. Satyapal for useful discussion. We thank Adam Block (Mount Lemmon SkyCenter/University of Arizona) for allowing us to publish his optical image of NGC 6286/NGC 6285. This research has made use of the *NuSTAR* Data Analysis Soft-

<sup>20</sup> 37% are composite AGN/starburst, 14% Seyfert 2s, 2% Sy1s and 6% LINERs.



**Table 3**

Summary of the X-ray spectral analysis for the spatially integrated X-ray spectrum of NGC 6286.

| PEXRAV   |                                 |                                 |                                 |
|--|---------------------------------|---------------------------------|---------------------------------|
| Column density ( $N_{\text{H}}$ ) [ $10^{22} \text{ cm}^{-2}$ ]  | $132^{+82}_{-54}$               |                                 |                                 |
| Reflection parameter ( $R$ )   | $\leq 0.4$                      |                                 |                                 |
| Plasma temperature ( $kT$ ) [keV]  | $0.79^A$                        |                                 |                                 |
| Scattered fraction ( $f_{\text{scatt}}$ ) [%]  | $1.3^{+1.9}_{-0.7} B$           |                                 |                                 |
| Fe K $\alpha$ EW [eV]  | $\leq 2318$                     |                                 |                                 |
| Observed 2–10 keV flux ( $F_{2-10}^{\text{obs}}$ ) [ $10^{-13} \text{ erg s}^{-1} \text{ cm}^{-2}$ ]   | 0.9                             |                                 |                                 |
| Observed 10–50 keV flux ( $F_{10-50}^{\text{obs}}$ ) [ $10^{-13} \text{ erg s}^{-1} \text{ cm}^{-2}$ ] | 9.6                             |                                 |                                 |
| Intrinsic 2–10 keV flux ( $F_{2-10}$ ) [ $10^{-12} \text{ erg s}^{-1} \text{ cm}^{-2}$ ]               | 2.6                             |                                 |                                 |
| intrinsic 10–50 keV flux ( $F_{10-50}$ ) [ $10^{-12} \text{ erg s}^{-1} \text{ cm}^{-2}$ ]             | 3.1                             |                                 |                                 |
| 2–10 keV luminosity ( $L_{2-10}$ ) [ $\text{erg s}^{-1}$ ]   | $2.01 \times 10^{42}$           |                                 |                                 |
| 10–50 keV luminosity ( $L_{10-50}$ ) [ $\text{erg s}^{-1}$ ]   | $2.34 \times 10^{42}$           |                                 |                                 |
| $\chi^2/\text{DOF}$  | 47.2/44                         |                                 |                                 |
| TORUS  |                                 |                                 |                                 |
|  | $\theta_{\text{OA}} = 40^\circ$ | $\theta_{\text{OA}} = 60^\circ$ | $\theta_{\text{OA}} = 80^\circ$ |
| Plasma temperature ( $kT$ ) [keV]  | $0.79^A$                        | $0.79^A$                        | $0.79^A$                        |
| Scattered fraction ( $f_{\text{scatt}}$ ) [%]  | $3.0^{+2.0}_{-1.3} B$           | $2.4^{+2.0}_{-1.3} B$           | $2.0^{+1.9}_{-1.3} B$           |
| Column density ( $N_{\text{H}}$ ) [ $10^{22} \text{ cm}^{-2}$ ]  | $110^{+89}_{-39}$               | $111^{+109}_{-41}$              | $106^{+101}_{-38}$              |
| Intrinsic 2–10 keV flux ( $F_{2-10}$ ) [ $10^{-13} \text{ erg s}^{-1} \text{ cm}^{-2}$ ]               | 10.7                            | 13.0                            | 16.0                            |
| intrinsic 10–50 keV flux ( $F_{10-50}$ ) [ $10^{-13} \text{ erg s}^{-1} \text{ cm}^{-2}$ ]             | 13.1                            | 15.8                            | 19.5                            |
| 2–10 keV luminosity ( $L_{2-10}$ ) [ $\text{erg s}^{-1}$ ]   | $8.14 \times 10^{41}$           | $9.84 \times 10^{41}$           | $1.21 \times 10^{42}$           |
| 10–50 keV luminosity ( $L_{10-50}$ ) [ $\text{erg s}^{-1}$ ]   | $9.90 \times 10^{41}$           | $1.20 \times 10^{42}$           | $1.48 \times 10^{42}$           |
| $\chi^2/\text{DOF}$  | 47.8/46                         | 48.1/46                         | 48.5/46                         |
| SPHERE   |                                 |                                 |                                 |
| Plasma temperature ( $kT$ ) [keV]  | $0.79^A$                        |                                 |                                 |
| Scattered fraction ( $f_{\text{scatt}}$ ) [%]  | $3.6^{+2.1}_{-1.2} B$           |                                 |                                 |
| Column density ( $N_{\text{H}}$ ) [ $10^{22} \text{ cm}^{-2}$ ]  | $101^{+46}_{-32}$               |                                 |                                 |
| Intrinsic 2–10 keV flux ( $F_{2-10}$ ) [ $10^{-13} \text{ erg s}^{-1} \text{ cm}^{-2}$ ]               | 9.2                             |                                 |                                 |
| intrinsic 10–50 keV flux ( $F_{10-50}$ ) [ $10^{-13} \text{ erg s}^{-1} \text{ cm}^{-2}$ ]             | 11.2                            |                                 |                                 |
| 2–10 keV luminosity ( $L_{2-10}$ ) [ $\text{erg s}^{-1}$ ]   | $6.98 \times 10^{41}$           |                                 |                                 |
| 10–50 keV luminosity ( $L_{10-50}$ ) [ $\text{erg s}^{-1}$ ]   | $8.50 \times 10^{41}$           |                                 |                                 |
| $\chi^2/\text{DOF}$  | 47.2/46                         |                                 |                                 |
| MYTORUS  |                                 |                                 |                                 |
| Photon index ( $\Gamma$ )  | $1.53^{+0.10}_{-NC} C$          |                                 |                                 |
| Plasma temperature ( $kT$ ) [keV]  | $0.79^A$                        |                                 |                                 |
| Scattered fraction ( $f_{\text{scatt}}$ ) [%]  | $8.8^{+4.9}_{-2.6} B$           |                                 |                                 |
| Column density ( $N_{\text{H}}$ ) [ $10^{22} \text{ cm}^{-2}$ ]  | $95^{+61}_{-39}$                |                                 |                                 |
| Intrinsic 2–10 keV flux ( $F_{2-10}$ ) [ $10^{-13} \text{ erg s}^{-1} \text{ cm}^{-2}$ ]               | 4.7                             |                                 |                                 |
| intrinsic 10–50 keV flux ( $F_{10-50}$ ) [ $10^{-13} \text{ erg s}^{-1} \text{ cm}^{-2}$ ]             | 11.1                            |                                 |                                 |
| 2–10 keV luminosity ( $L_{2-10}$ ) [ $\text{erg s}^{-1}$ ]   | $3.49 \times 10^{41}$           |                                 |                                 |
| 10–50 keV luminosity ( $L_{10-50}$ ) [ $\text{erg s}^{-1}$ ]   | $8.35 \times 10^{41}$           |                                 |                                 |
| $\chi^2/\text{DOF}$  | 52.5/45                         |                                 |                                 |

**Notes.** <sup>A</sup> parameter left free to vary within the uncertainties of the value obtained fitting the extended emission (see § 4.2 for details). <sup>B</sup> value calculated from the ratio of  $n_{\text{po}}$  and  $n_{\text{po}}^{\text{scatt}}$ . <sup>C</sup> the photon index in MyTORUS is calculated only in the range  $\Gamma = 1.4 - 2.6$ .

ware (NuSTARDAS) jointly developed by the ASI Science Data Center (ASDC, Italy) and the California Institute of Technology (Caltech, USA), and of the NASA/IPAC Infrared Science Archive and NASA/IPAC Extragalactic Database (NED), which are operated by the Jet Propulsion Laboratory, California Institute of Technology, under contract with the National Aeronautics and Space Administration. We acknowledge financial support from the CONICYT-Chile grants “EMBIGGEN” Anillo ACT1101 (CR, FEB, ET), FONDECYT 1141218 (CR, FEB), FONDECYT 315238 (CRC), FONDECYT 3150361 (GP), Basal-CATA PFB-06/2007 (CR, FEB, ET), the NASA *NuSTAR* AO1 Award NNX15AV27G (FEB) and the Ministry of Economy, Development, and Tourism’s Millennium Science Initiative through grant IC120009, awarded to The Millennium Institute of Astrophysics, MAS (FEB, CRC). KS gratefully acknowledges support from Swiss National Science Foundation Grant PP00P2\_138979/1. MI was supported by JSPS KAKENHI Grant Number 23540273 and 15K05030.

*Facilities:* NuSTAR, Chandra, Swift, XMM-Newton.

## REFERENCES

- Aalto, S., Costagliola, S. M. F., Gonzalez-Alfonso, E., et al. 2015, ArXiv e-prints
- Abel, N. P., & Satyapal, S. 2008, *ApJ*, 678, 686
- Alexander, D. M., Chary, R.-R., Pope, A., et al. 2008, *ApJ*, 687, 835
- Alonso-Herrero, A., Pereira-Santaella, M., Rieke, G. H., & Rigopoulou, D. 2012, *ApJ*, 744, 2
- Annuar, A., Gandhi, P., Alexander, D. M., et al. 2015, *ApJ*, 815, 36
- Arévalo, P., Bauer, F. E., Puccetti, S., et al. 2014, *ApJ*, 791, 81
- Armus, L., Mazzarella, J. M., Evans, A. S., et al. 2009, *PASP*, 121, 559
- Arnaud, K. A. 1996, in *Astronomical Society of the Pacific Conference Series*, Vol. 101, *Astronomical Data Analysis Software and Systems V*, ed. G. H. Jacoby & J. Barnes, 17
- Asmus, D., Gandhi, P., Hoenig, S. F., Smette, A., & Duschl, W. J. 2015, ArXiv e-prints
- Assef, R. J., Eisenhardt, P. R. M., Stern, D., et al. 2015, *ApJ*, 804, 27
- Baan, W. A., Salzer, J. J., & LeWinter, R. D. 1998, *ApJ*, 509, 633
- Baldwin, J. A., Phillips, M. M., & Terlevich, R. 1981, *PASP*, 93, 5
- Baloković, M., Comastri, A., Harrison, F. A., et al. 2014, *ApJ*, 794, 111
- Bauer, F. E., Yan, L., Sajina, A., & Alexander, D. M. 2010, *ApJ*, 710, 212
- Bauer, F. E., Arévalo, P., Walton, D. J., et al. 2015, *ApJ*, 812, 116
- Becker, R. H., White, R. L., & Helfand, D. J. 1995, *ApJ*, 450, 559
- Brightman, M., & Nandra, K. 2011, *MNRAS*, 413, 1206
- Burrows, D. N., Hill, J. E., Nousek, J. A., et al. 2005, *Space Sci. Rev.*, 120, 165
- Caputi, K. I., Lagache, G., Yan, L., et al. 2007, *ApJ*, 660, 97
- Caramete, L. I., & Biermann, P. L. 2010, *A&A*, 521, A55
- Cash, W. 1979, *ApJ*, 228, 939
- Condon, J. J. 1992, *ARA&A*, 30, 575
- Condon, J. J., Cotton, W. D., Greisen, E. W., et al. 1998, *AJ*, 115, 1693
- Condon, J. J., Huang, Z.-P., Yin, Q. F., & Thuan, T. X. 1991, *ApJ*, 378, 65
- Di Matteo, T., Springel, V., & Hernquist, L. 2005, *Nature*, 433, 604
- Donley, J. L., Koekemoer, A. M., Brusa, M., et al. 2012, *ApJ*, 748, 142
- Dudik, R. P., Satyapal, S., & Marcu, D. 2009, *ApJ*, 691, 1501
- Eisenhardt, P. R. M., Wu, J., Tsai, C.-W., et al. 2012, *ApJ*, 755, 173
- Franceschini, A., Baito, V., Persic, M., et al. 2003, *MNRAS*, 343, 1181
- Gabor, J. M., Capelo, P. R., Volonteri, M., et al. 2015, ArXiv e-prints
- Gabriel, C., Denby, M., Fyfe, D. J., et al. 2004, in *Astronomical Society of the Pacific Conference Series*, Vol. 314, *Astronomical Data Analysis Software and Systems (ADASS) XIII*, ed. F. Ochsenbein, M. G. Allen, & D. Egret, 759
- Gandhi, P., Hönig, S. F., & Kishimoto, M. 2015, *ApJ*, 812, 113
- Gandhi, P., Horst, H., Smette, A., et al. 2009, *A&A*, 502, 457
- Gandhi, P., Lansbury, G. B., Alexander, D. M., et al. 2014, *ApJ*, 792, 117
- Garmire, G. P., Bautz, M. W., Ford, P. G., Nousek, J. A., & Ricker, Jr., G. R. 2003, in *Society of Photo-Optical Instrumentation Engineers (SPIE) Conference Series*, Vol. 4851, *X-Ray and Gamma-Ray Telescopes and Instruments for Astronomy*, ed. J. E. Truemper & H. D. Tananbaum, 28–44
- Gehrels, N., Chincarini, G., Giommi, P., et al. 2004, *ApJ*, 611, 1005
- Georgakakis, A., Rowan-Robinson, M., Nandra, K., et al. 2010, *MNRAS*, 406, 420
- Georgantopoulos, I., Rovilos, E., Akylas, A., et al. 2011a, *A&A*, 534, A23
- Georgantopoulos, I., Dasyra, K. M., Rovilos, E., et al. 2011b, *A&A*, 531, A116
- Glikman, E., Simmons, B., Mailly, M., et al. 2015, *ApJ*, 806, 218
- Goto, T., Takagi, T., Matsuhara, H., et al. 2010, *A&A*, 514, A6
- Goulding, A. D., & Alexander, D. M. 2009, *MNRAS*, 398, 1165
- Harrison, F. A., Craig, W. W., Christensen, F. E., et al. 2013, *ApJ*, 770, 103
- Helou, G., Soifer, B. T., & Rowan-Robinson, M. 1985, *ApJ*, 298, L7
- Ho, L. C. 2008, *ARA&A*, 46, 475
- Howell, J. H., Armus, L., Mazzarella, J. M., et al. 2010, *ApJ*, 715, 572
- Ichikawa, K., Imanishi, M., Ueda, Y., et al. 2014, *ApJ*, 794, 139
- Imanishi, M. 2009, *ApJ*, 694, 751
- Imanishi, M., & Dudley, C. C. 2000, *ApJ*, 545, 701
- Imanishi, M., Maiolino, R., & Nakagawa, T. 2010a, *ApJ*, 709, 801
- Imanishi, M., Nakagawa, T., Shirahata, M., Ohyama, Y., & Onaka, T. 2010b, *ApJ*, 721, 1233
- Imanishi, M., Nakanishi, K., Tamura, Y., Oi, N., & Kohno, K. 2007, *AJ*, 134, 2366
- Imanishi, M., Terashima, Y., Anabuki, N., & Nakagawa, T. 2003, *ApJ*, 596, L167
- Inami, H., Armus, L., Charmandaris, V., et al. 2013, *ApJ*, 777, 156
- Iwasawa, K., Sanders, D. B., Evans, A. S., et al. 2009, *ApJ*, 695, L103
- Iwasawa, K., Sanders, D. B., Teng, S. H., et al. 2011, *A&A*, 529, A106
- Jansen, F., Lumb, D., Altieri, B., et al. 2001, *A&A*, 365, L1
- Kalberla, P. M. W., Burton, W. B., Hartmann, D., et al. 2005, *A&A*, 440, 775
- Kartaltepe, J. S., Sanders, D. B., Le Floc’h, E., et al. 2010, *ApJ*, 709, 572
- Kewley, L. J., Groves, B., Kauffmann, G., & Heckman, T. 2006, *MNRAS*, 372, 961
- Kleinmann, D. E., & Low, F. J. 1970, *ApJ*, 159, L165
- Koss, M., Mushotzky, R., Baumgartner, W., et al. 2013, *ApJ*, 765, L26
- Koss, M. J., Romero-Cañizales, C., Baronchelli, L., et al. 2015, *ApJ*, 807, 149
- La Franca, F., Melini, G., & Fiore, F. 2010, *ApJ*, 718, 368
- Lacy, M., Storrie-Lombardi, L. J., Sajina, A., et al. 2004, *ApJS*, 154, 166
- Lansbury, G. B., Gandhi, P., Alexander, D. M., et al. 2015, *ApJ*, 809, 115
- Le Floc’h, E., Papovich, C., Dole, H., et al. 2005, *ApJ*, 632, 169
- Low, J., & Kleinmann, D. E. 1968, *AJ*, 73, 868
- Lutz, D., Veilleux, S., & Genzel, R. 1999, *ApJ*, 517, L13
- Madsen, K. K., Harrison, F. A., Markwardt, C., et al. 2015, ArXiv e-prints
- Magdziarz, P., & Zdziarski, A. A. 1995, *MNRAS*, 273, 837
- Magorrian, J., Tremaine, S., Richstone, D., et al. 1998, *AJ*, 115, 2285
- Mullaney, J. R., Alexander, D. M., Goulding, A. D., & Hickox, R. C. 2011, *MNRAS*, 414, 1082
- Murphy, E. J. 2013, *ApJ*, 777, 58

- Murphy, K. D., & Yaqoob, T. 2009, *MNRAS*, 397, 1549
- Nagar, N. M., Falcke, H., & Wilson, A. S. 2005, *A&A*, 435, 521
- Nandra, K., & Pounds, K. A. 1994a, *MNRAS*, 268, 405
- . 1994b, *MNRAS*, 268, 405
- Nardini, E., Risaliti, G., Salvati, M., et al. 2008, *MNRAS*, 385, L130
- Nardini, E., Risaliti, G., Watabe, Y., Salvati, M., & Sani, E. 2010, *MNRAS*, 405, 2505
- Panessa, F., Barcons, X., Bassani, L., et al. 2007, *A&A*, 467, 519
- Parra, R., Conway, J. E., Aalto, S., et al. 2010, *ApJ*, 720, 555
- Pereira-Santaella, M., Alonso-Herrero, A., Santos-Lleo, M., et al. 2011, *A&A*, 535, A93
- Petric, A. O., Armus, L., Howell, J., et al. 2011, *ApJ*, 730, 28
- Piconcelli, E., Jimenez-Bailón, E., Guainazzi, M., et al. 2005, *A&A*, 432, 15
- Privon, G. C., Herrero-Illana, R., Evans, A. S., et al. 2015, *ArXiv e-prints*
- Ptak, A., Heckman, T., Levenson, N. A., Weaver, K., & Strickland, D. 2003, *ApJ*, 592, 782
- Ptak, A., Hornschemeier, A., Zezas, A., et al. 2015, *ApJ*, 800, 104
- Puccetti, S., Comastri, A., Bauer, F. E., et al. 2015, *ArXiv e-prints*
- Ricci, C., Ueda, Y., Ichikawa, K., et al. 2014a, *A&A*, 567, A142
- Ricci, C., Ueda, Y., Koss, M. J., et al. 2015, *ApJ*, 815, L13
- Ricci, C., Ueda, Y., Paltani, S., et al. 2014b, *MNRAS*, 441, 3622
- Ricci, C., Walter, R., Courvoisier, T. J.-L., & Paltani, S. 2011, *A&A*, 532, A102
- Risaliti, G., Imanishi, M., & Sani, E. 2010, *MNRAS*, 401, 197
- Risaliti, G., Maiolino, R., Marconi, A., et al. 2006, *MNRAS*, 365, 303
- Romero-Cañizales, C., Pérez-Torres, M. Á., & Alberdi, A. 2012a, *MNRAS*, 422, 510
- Romero-Cañizales, C., Pérez-Torres, M. A., Alberdi, A., et al. 2012b, *A&A*, 543, A72
- Rovilos, E., Georgantopoulos, I., Akyas, A., et al. 2014, *MNRAS*, 438, 494
- Sanders, D. B., Egami, E., Lipari, S., Mirabel, I. F., & Soifer, B. T. 1995, *AJ*, 110, 1993
- Sanders, D. B., Mazzarella, J. M., Kim, D.-C., Surace, J. A., & Soifer, B. T. 2003, *AJ*, 126, 1607
- Sanders, D. B., & Mirabel, I. F. 1996, *ARA&A*, 34, 749
- Sanders, D. B., Soifer, B. T., Elias, J. H., et al. 1988, *ApJ*, 325, 74
- Sani, E., Risaliti, G., Salvati, M., et al. 2008, *ApJ*, 675, 96
- Sarzi, M., Shields, J. C., Schawinski, K., et al. 2010, *MNRAS*, 402, 2187
- Satyapal, S., Vega, D., Dudik, R. P., Abel, N. P., & Heckman, T. 2008, *ApJ*, 677, 926
- Satyapal, S., Vega, D., Heckman, T., O'Halloran, B., & Dudik, R. 2007, *ApJ*, 663, L9
- Schawinski, K., Simmons, B. D., Urry, C. M., Treister, E., & Glikman, E. 2012, *MNRAS*, 425, L61
- Shepherd, M. C., Pearson, T. J., & Taylor, G. B. 1995, in *Bulletin of the American Astronomical Society*, Vol. 27, *Bulletin of the American Astronomical Society*, ed. B. J. Butler & D. O. Muhleman, 903
- Shu, X. W., Yaqoob, T., & Wang, J. X. 2010, *ApJS*, 187, 581
- Soto, K. T., & Martin, C. L. 2010, *ApJ*, 716, 332
- . 2012, *ApJS*, 203, 3
- Soto, K. T., Martin, C. L., Prescott, M. K. M., & Armus, L. 2012, *ApJ*, 757, 86
- Springel, V., Di Matteo, T., & Hernquist, L. 2005, *MNRAS*, 361, 776
- Stern, D. 2015, *ApJ*, 807, 129
- Stern, D., Eisenhardt, P., Gorjian, V., et al. 2005, *ApJ*, 631, 163
- Stern, D., Lansbury, G. B., Assef, R. J., et al. 2014, *ApJ*, 794, 102
- Stierwalt, S., Armus, L., Surace, J. A., et al. 2013, *ApJS*, 206, 1
- Stierwalt, S., Armus, L., Charmandaris, V., et al. 2014, *ApJ*, 790, 124
- Strüder, L., Briel, U., Dennerl, K., et al. 2001, *A&A*, 365, L18
- Sturm, E., Lutz, D., Verma, A., et al. 2002, *A&A*, 393, 821
- Szokoly, G. P., Bergeron, J., Hasinger, G., et al. 2004, *ApJS*, 155, 271
- Teng, S. H., Wilson, A. S., Veilleux, S., et al. 2005, *ApJ*, 633, 664
- Teng, S. H., Veilleux, S., Anabuki, N., et al. 2009, *ApJ*, 691, 261
- Teng, S. H., Brandt, W. N., Harrison, F. A., et al. 2014, *ApJ*, 785, 19
- Teng, S. H., Rigby, J. R., Stern, D., et al. 2015, *ArXiv e-prints*
- Terashima, Y., & Wilson, A. S. 2003, *ApJ*, 583, 145
- Treister, E., Natarajan, P., Sanders, D. B., et al. 2010a, *Science*, 328, 600
- Treister, E., Schawinski, K., Urry, C. M., & Simmons, B. D. 2012, *ApJ*, 758, L39
- Treister, E., Urry, C. M., Schawinski, K., Cardamone, C. N., & Sanders, D. B. 2010b, *ApJ*, 722, L238
- Turner, M. J. L., Abbey, A., Arnaud, M., et al. 2001, *A&A*, 365, L27
- U, V., Sanders, D. B., Mazzarella, J. M., et al. 2012, *ApJS*, 203, 9
- Ueda, Y., Akiyama, M., Hasinger, G., Miyaji, T., & Watson, M. G. 2014, *ApJ*, 786, 104
- Vardoulaki, E., Charmandaris, V., Murphy, E. J., et al. 2015, *A&A*, 574, A4
- Vasudevan, R. V., & Fabian, A. C. 2007, *MNRAS*, 381, 1235
- Vega, O., Clemens, M. S., Bressan, A., et al. 2008, *A&A*, 484, 631
- Veilleux, S., Kim, D.-C., & Sanders, D. B. 1999, *ApJ*, 522, 113
- Veilleux, S., Kim, D.-C., Sanders, D. B., Mazzarella, J. M., & Soifer, B. T. 1995, *ApJS*, 98, 171
- Veilleux, S., & Osterbrock, D. E. 1987, *ApJS*, 63, 295
- Veilleux, S., Rupke, D. S. N., Kim, D.-C., et al. 2009, *ApJS*, 182, 628
- Vignati, P., Molendi, S., Matt, G., et al. 1999, *A&A*, 349, L57
- Weedman, D. W., Hao, L., Higdon, S. J. U., et al. 2005, *ApJ*, 633, 706
- Weisskopf, M. C., Tananbaum, H. D., Van Speybroeck, L. P., & O'Dell, S. L. 2000, in *Society of Photo-Optical Instrumentation Engineers (SPIE) Conference Series*, Vol. 4012, *X-Ray Optics, Instruments, and Missions III*, ed. J. E. Truemper & B. Aschenbach, 2–16
- Wilms, J., Allen, A., & McCray, R. 2000, *ApJ*, 542, 914
- Wu, J., Tsai, C.-W., Sayers, J., et al. 2012, *ApJ*, 756, 96
- Yaqoob, T. 2012, *MNRAS*, 423, 3360
- Yuan, T.-T., Kewley, L. J., & Sanders, D. B. 2010, *ApJ*, 709, 884
- Yun, M. S., Reddy, N. A., & Condon, J. J. 2001, *ApJ*, 554, 803